Shear viscosity of dilute suspensions of ellipsoidal particles with a lattice Boltzmann method

Haibo Huang, YanFeng Wu, and Xiyun Lu
Department of Modern Mechanics, University of Science and Technology of China, Hefei, Anhui 230026, China
(Received 21 March 2012; published 8 October 2012)

The intrinsic viscosities for prolate and oblate spheroidal suspensions in a dilute Newtonian fluid are studied using a three-dimensional lattice Boltzmann method. Through directly calculated viscous dissipation, the minimum and maximum intrinsic viscosities and the period of the tumbling state all agree well with the analytical solution for particles with different aspect ratios. This numerical test verifies the analysis on maximum and minimum intrinsic viscosities. Different behavior patterns of transient intrinsic viscosity in a period are analyzed in detail. A phase lag between the transient intrinsic viscosity and the orientation of the particle at finite Reynolds number (Re) is found and attributed to fluid and particle inertia. At lower Re, the phase lag increases with Re. There exists a critical Reynolds number Re_a at which the phase lag begins to decrease with Re. The Re_a depends on the aspect ratio of the particle. We found that both the intrinsic viscosity and the period change linearly with Re when $\mathrm{Re} < \mathrm{Re}_a$ (low-Re regime) and nonlinearly when $\mathrm{Re} > \mathrm{Re}_a$ (high-Re regime). In the high-Re regime, the dependence of the period on Re is consistent with a scaling law, and the dependence of the intrinsic viscosity on Re is well described by second-degree polynomial fits.

DOI: 10.1103/PhysRevE.86.046305 PACS number(s): 47.55.Kf, 47.11.−j

I. INTRODUCTION

Suspended particles in flows occur in many applications and play an important role in industry. For example, the behavior of suspended particles may affect the quality of paper [1]. Shear viscosity of dilute suspensions of spheres has been studied analytically by Einstein [2]. According to the theory, the relative viscosity $\langle\bar{\pi}\rangle$ in dilute suspensions of spheres is [2] $\langle\bar{\pi}\rangle = 1 + \phi\langle\bar{\eta}\rangle$, where ϕ is the solid volume fraction and $\langle\bar{\eta}\rangle = \frac{5}{2}$ is the intrinsic viscosity. The relative viscosity $\langle\bar{\pi}\rangle$ is defined as the ratio of the effective suspension viscosity ν_s to the corresponding viscosity of the pure fluid ν_f, i.e., $\langle\bar{\pi}\rangle \equiv \frac{\nu_s}{\nu_f}$. The intrinsic viscosity is defined as $\langle\bar{\eta}\rangle = \frac{\langle\bar{\pi}\rangle - 1}{\phi}$. Later, Krieger and Dougherty [3] extended Einstein's formula to a larger ϕ regime semiempirically. Recently, Lishchuk *et al.* [4] studied the shear viscosity of bulk suspensions of spherical particles at a low Reynolds number (Re) using a lattice Boltzmann (LB) method. In their result, they included a correction for the effective hydrodynamic radius of particles due to the simple bounce-back scheme they used [4]. In the present study, such corrections are not necessary.

For a dilute suspension of nonspherical ellipsoidal particles, the variation of intrinsic viscosity would be more complex. The rotational behavior of prolate or oblate spheroids at very low Reynolds numbers has been studied theoretically for a long time. Jeffery investigated the motion of a single ellipsoid in shear flow while completely neglecting inertial effects [5]. He concluded that the final rotational state of an ellipsoid cannot be determined because it depends on initial conditions. To definitively determine the final rotational state, Jeffery [5] hypothesized that, "The particle will tend to adopt that motion which, of all the motions possible under the approximated equations, corresponds to the least dissipation of energy." Extensive analytical investigations [6] studied the inertial effect at $\mathrm{Re} < 1$ using perturbation theory. However, their analysis is not applicable to large-Re cases. Leal [7] reviewed most of the previous relevant theoretical studies. There are also some relevant experimental works in the literature. Taylor [8] confirmed Jeffery's hypothesis by investigating the orbit of a prolate or oblate spheroid in a Couette flow at a very low Reynolds number. However, Karnis *et al.* [9] found that even when the inertial effect is very small [e.g., at $\mathrm{ReO}(10^{-3})$], nonspherical particles may adopt a motion that is different from Jeffery's hypothesis. For suspensions of many spherical particles, states of maximum dissipation have been observed experimentally [10].

Different numerical methods have also been used to study the motion of particles in flows. However, some methods such as Stokesian dynamics [11] are only applicable to spherical particles and they neglect the inertial term, which may have a significant influence on the motion of particles. For finite-Reynolds-number flows, the Navier-Stokes equations have to be solved. Feng *et al.* [12] simulated the motion of a single ellipse in two-dimensional (2D) creeping flows using a finite element approach. They confirmed Jeffery's hypothesis at $\mathrm{Re} \approx 1$. In the past 30 years, the lattice Boltzmann methods (LBMs) have been developed into an efficient numerical tool to study particulate suspensions [1,4,13–15]. Qi and Luo studied the energy dissipation of a prolate spheroid at $\mathrm{Re} = 0.1$ and 18 using a LBM [1]. According to their study, the numerical results did not support Jeffery's hypothesis. However, the calculated intrinsic viscosities in their study [1] seem not to be consistent with Jeffery's study [5]. That will be illustrated in Sec. III in detail. Here we demonstrate that our results are much more reliable than those of Qi and Luo [1] and further confirm that Jeffery's hypothesis may be incorrect.

Some numerical studies investigated prolate and oblate spheroid suspensions in 3D Couette flows for Re up to approximately several hundred [1,15,16]. They focused on the critical transition Re for different rotational modes, which may depend on the initial orientation [15]. There are also some studies that focused on the critical Re at which the particle would stop rotating [14]. Lin *et al.* [17] studied the inertial effects on the suspension of a rigid sphere in a simple shear flow. They proposed a formula for the suspension viscosity: $\nu_s = \nu_f[1 + \phi(\frac{5}{2} + 1.34\,\mathrm{Re}^{1.5})]$. However, for suspensions of

elliptical spheroids, no such formula is proposed. Here, from our numerical results, we propose to separate the dependences of the intrinsic viscosity and the period of the tumbling state on Re into two regimes. In the low-Re and high-Re regimes, they change linearly and nonlinearly with Re, respectively. The phase lag between the transient intrinsic viscosity and the orientation of the particle at finite Reynolds number is also analyzed in detail.

In this study, we focus on the intrinsic viscosity of spheroids in a 3D Couette flow for Re up to about 200. The numerical method used in our study is based on the LBM [13,14] with improvements in the collision model [18] and curved-wall boundary treatment [18]. For the collision model, the multi-relaxation-time (MRT) model [18] is used because it has better numerical stability. For the curved-wall boundary condition, an accurate momentum-exchange-based scheme [18] is applied. The translational and orientational motions of the spheroid are modeled by the Newtonian and Euler equations, respectively. Our scheme for calculating relative viscosity was validated in Ref. [15]. The present work is intended to provide a better understanding of the intrinsic viscosity of dilute suspensions of nonspherical particles. In Sec. II, the LBM and the basic equations for the motion of a solid particle are introduced briefly. Results and discussion on the shear viscosity of dilute suspensions of ellipsoidal particles with different Re and aspect ratios are described in Sec. III. Conclusions are presented in Sec. IV.

II. NUMERICAL METHOD

In our study, the fluid flow is solved by the MRT-LBM [18]. The following MRT lattice Boltzmann equation (LBE) [19] is employed to solve the incompressible Navier-Stokes equations:

$$|f(\mathbf{x}+\mathbf{e}_i\delta t, t+\delta t)\rangle - |f(\mathbf{x},t)\rangle = -M^{-1}\hat{\mathbf{S}}[|m(\mathbf{x},\mathbf{t})\rangle - |\mathbf{m}^{(\mathrm{eq})}(\mathbf{x},\mathbf{t})\rangle], \quad (1)$$

where the Dirac notation of ket $|\cdot\rangle$ vectors symbolizes the column vectors. The particle distribution function $|f(\mathbf{x},t)\rangle$ has 19 components f_i with $i = 0,1,2,3,\ldots,18$ in our 3D simulations because the D3Q19 velocity model is used. The collision matrix $\hat{\mathbf{S}} = MSM^{-1}$ is diagonal with $\hat{\mathbf{S}}$ [19],

$$\hat{\mathbf{S}} \equiv \mathrm{diag}(0, s_1, s_2, 0, s_4, 0, s_4, 0, s_4, s_9, s_{10}, s_9, s_{10}, s_{13}, s_{13}, s_{13}, s_{16}, s_{16}, s_{16}).$$

$|m^{(\mathrm{eq})}\rangle$ is the equilibrium value of the moment $|m\rangle$. The 19×19 matrix M [19] is a linear transformation which is used to map a vector $|f\rangle$ in discrete velocity space to a vector $|m\rangle$ in moment space, i.e., $|m\rangle = M|f\rangle$, $|f\rangle = M^{-1}|m\rangle$. In the above equation, $\mathbf{e}_i$ are the discrete velocities of the D3Q19 model. The lattice speed is defined as $c = \frac{\delta x}{\delta t}$, where δx and δt are the lattice spacing and time step, respectively, in LB simulations. The matrix M, the discrete velocities of the D3Q19 model, and $|m^{(\mathrm{eq})}\rangle$ are all identical to those in Refs. [15,19].

The macrovariable density ρ and momentum j_ζ are obtained from

$$\rho = \sum_i f_i, \quad j_\zeta = \sum_i f_i e_{i\zeta}, \quad (2)$$

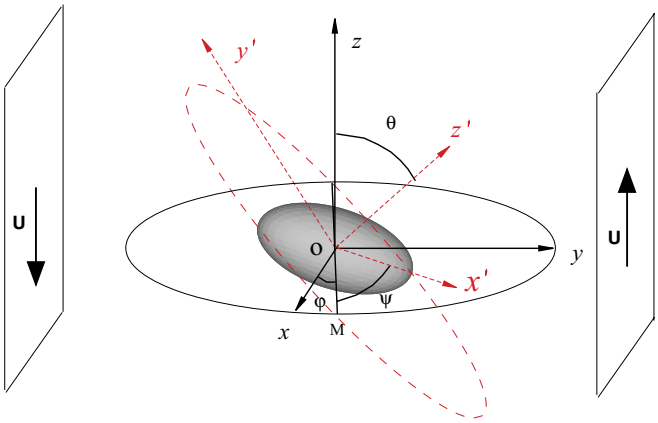

FIG. 1. (Color online) Schematic diagram of a spheroid with its symmetry axis in the x' direction in a Couette flow. Line OM represents the intersection of the (x,y) and the (x',y') coordinate planes. The two walls at $y = -L$ and L move in opposite directions. Periodic boundary conditions are applied in the x and z directions.

where ζ denotes x, y, or z coordinates. Here the collision process is executed in moment space [19]. In our simulations, the parameters are chosen as $s_1 = 1.19$, $s_2 = s_{10} = 1.4$, $s_4 = 1.2$, $s_9 = \frac{1}{\tau}$, $s_{13} = s_9$, and $s_{16} = 1.98$. The parameter τ is relevant to the kinematic viscosity of the fluid with $\nu_f = c_s^2(\tau - 0.5)\delta t$ and $c_s = \frac{c}{\sqrt{3}}$. The pressure in the flow field can be obtained from the density via the equation of state $p = c_s^2\rho$.

The particle's movement and rotation are updated at each time step through Newton's law and Euler equations. The prolate or oblate spheroid is described by

$$\frac{x'^2}{a^2} + \frac{y'^2}{b^2} + \frac{z'^2}{c^2} = 1, \quad (3)$$

where (x',y',z') represents the body-fixed coordinate system and a, b, and c are the lengths of three semiprincipal axes of a spheroid in the x', y', and z' directions, respectively. The spatial orientation of any body-fixed frame (coordinate system) can be obtained by a composition of rotations around the z'-x'-z' axis with Euler angles (φ,θ,ψ) from the space-fixed frame (x,y,z) that initially overlaps the body-fixed frame. The composition of rotations is illustrated in Fig. 1. Noted that the symmetry axis of the spheroid is in the x' direction.

The translational velocity $\mathbf{U}(t)$ of the solid particle is determined by solving Newton's equations [15]. The rotation of the spheroid is determined by Euler equations, which are written as

$$\mathbf{I}\cdot\frac{d\mathbf{\Omega}(t)}{dt} + \mathbf{\Omega}(t)\times[\mathbf{I}\cdot\mathbf{\Omega}(t)] = \mathbf{T}(t), \quad (4)$$

where $\mathbf{I}$ is the inertial tensor. Note that in the body-fixed coordinate system [coordinates (x',y',z') in Fig. 1], the tensor is diagonal and the principal moments of inertia are $I_{x'x'} = m\frac{b^2+c^2}{5}$, $I_{y'y'} = m\frac{a^2+c^2}{5}$, and $I_{z'z'} = m\frac{a^2+b^2}{5}$, where $m = \rho_0\frac{4}{3}\pi abc$ is the mass of the suspended particle. The $\mathbf{\Omega}$ represent angular velocities and $\mathbf{T}$ is the torque exerted on the solid particle in the same coordinate system. Here four quaternion parameters [15] are used as generalized coordinates to solve the corresponding system of equations. With the

quaternion formulation, Ω in [Eq. (4)] can be solved using a fourth-order accurate Runge-Kutta integration procedure [15].

The fluid-solid coupling in our study is based on the schemes in Refs. [13] and [18]. The force on solid boundary nodes is calculated through the momentum exchange scheme [18,20], and the force due to the fluid particle entering and leaving the solid region [13] is also considered.

A. Rotational modes and parameters in simulations

In the space-fixed coordinates, the streamwise direction of the Couette flow is along the z direction. The velocity gradient and the vorticity are oriented in the y and x directions, respectively. The tumbling mode indicates a particle rotation about its y' or z' axis with the axis parallel to the vorticity direction. The log rolling mode indicates the spheroid spin around the evolution axis (the x' axis), which overlaps the x axis.

To describe the geometry of the spheroid, "ellipticity" is defined here to be the difference of the greatest and least diameters divided by the greatest, i.e., $\varepsilon = \frac{a-b}{a}$ for a prolate spheroid and $\varepsilon = \frac{b-a}{b}$ for an oblate spheroid [5]. The computational domain in all of our following simulations has dimension $2L$ in the x, y, and z directions. Two walls located at $y = -L$ and L move in opposite directions with speed U, as shown in Fig. 1. Periodic boundary conditions are applied in both the x and z directions. To calculate the force acting on the spheroid more accurately, grid refinement is used near the particle. Both the fine grid and the particle are located in the center of the domain, and the particle is immersed in the fine grid. We use 1 $l.u.$ and 1 $t.s.$ to denote 1 Δx_f and 1 Δt_f, respectively. The fine grid has dimension L in three directions with lattice spacing 1 $l.u.$ The rest of the computational domain is filled with coarse mesh and the lattice spacing $\Delta x_c = 2$ $l.u.$ and $\Delta t_c = 2$ $t.s.$ The fine and coarse grids are coupled using the scheme proposed by Filippova *et al.* [21].

The particle Reynolds number is defined to be $\mathrm{Re} = \frac{4Gd^2}{\nu_f}$, where $G = \frac{U}{L}$ and d is the length of the semimajor axis (i.e., $d = a$ for the prolate spheroid and $d = b = c$ for the oblate spheroid). In all of our cases, the confinement ratio $\frac{L}{a} > 5$ and the volume fraction is less than 0.7%. Hence, the moving wall effect can be neglected and the suspensions of particles can be regarded as dilute suspensions.

In our simulations, the flow is intended to be incompressible. To ensure the incompressibility condition, the maximum velocity in the flow field should not exceed 0.1 $l.u./t.s.$ [15]. On the other hand, to ensure that the bounce-back boundary condition correctly mimics the nonslip boundary condition on the wall, τ used in the simulations should not be too large. τ_f and τ_c are the relaxation times in the fine mesh and coarse mesh, respectively. They satisfy the formula $\frac{1}{3}(\tau_f - 0.5)\Delta t_f = \frac{1}{3}(\tau_c - 0.5)\Delta t_c$. In our simulations, we adopt $\tau_f < 1.3$; hence the bounce back can correctly recover the nonslip physical boundary condition. Considering the above two effects, the parameters are chosen in the following way. For the low Reynolds number cases, U is calculated from the definition of Re. For example, in the case of $\mathrm{Re} = 0.5$, $L = 192$ $l.u.$, $a = 24$ $l.u.$, $b = c = 12$ $l.u.$, τ_f is set to be 1.2, and the calculated velocity of the wall is 0.004 86 $l.u./t.s.$ For larger Reynolds number cases, U is kept at 0.1 $l.u./t.s.$ and τ_f is calculated from the definition of Re. For example, in the case of a prolate spheroid with $\mathrm{Re} = 30$, the parameters are $L = 192$ $l.u.$, $a = 24$ $l.u.$, $b = c = 12$ $l.u.$, and the calculated τ_f and τ_c are 0.74 and 0.62, respectively.

In all of our numerical tests, the velocity field was initialized as a Couette flow with a uniform pressure field ($p_0 = c_s^2\rho_0$). The particle is released at the center of the computational domain with zero velocity. Although the translational motion of the particle is not constrained, the spheroid center is not found to depart from the center of the computational domain in all simulated cases. To make the particle enter log rolling mode and tumbling mode quickly, it was excited by setting the initial orientation as $(\varphi_0,\theta_0,\psi_0) = (0^\circ,0^\circ,0^\circ)$ and $(\varphi_0,\theta_0,\psi_0) = (90^\circ,90^\circ,90^\circ)$, respectively.

B. Calculation of the intrinsic viscosity

From Fig. 1, we can see that the streamlines of the Couette flow are in the z direction and that the velocity gradient is in the y direction. The shear stress at a fluid node $\mathbf{x}$ can be obtained through $\sigma(\mathbf{x}) = \rho\nu_f(\partial_y w + \partial_z v)$, where v and w are the velocity components in the y and z directions at $\mathbf{x}$, respectively. We note that in the MRT LBM, the second-order moments of the distribution function are given by $p_{yz} = \Sigma_i e_{iy}e_{iz}f_i = \rho vw - \tau c_s^2\rho(\partial_y w + \partial_z v)$. Therefore, at each fluid node the shear stress is obtained through

$$\sigma(\mathbf{x}) = \rho\nu_f(\partial_y w + \partial_z v) = \frac{\nu_f}{\tau c_s^2}(\rho vw - p_{yz}). \tag{5}$$

In the lattice Bhatnagar-Gross-Krook (BGK) method, at each fluid node the shear stress can be obtained by $\sigma(\mathbf{x}) = \rho\nu_f(\partial_y w + \partial_z v) = -(1 - \frac{1}{2\tau})\sum f_i^{neq}e_{iy}e_{iz}$, where $f_i^{neq} = f_i - f_i^{eq}$.

The energy dissipation represented by the relative viscosity $\langle\bar{\pi}\rangle$ of the flow system [1] is given by

$$\langle\bar{\pi}\rangle = \frac{\langle\bar{\sigma}\rangle}{\rho\nu_f G}, \tag{6}$$

where $\langle\bar{\sigma}\rangle$ is the temporally and spatially averaged shear stress and G is the shear rate of the Couette flow without particles. The transient intrinsic viscosity is defined to be

$$\langle\eta(t)\rangle = \frac{\langle\pi(t)\rangle - 1}{\phi}, \tag{7}$$

where $\langle\pi(t)\rangle = \frac{\langle\sigma(t)\rangle}{\rho\nu_f G}$ and $\langle\sigma(t)\rangle$ is the spatially averaged shear stress at time t.

To calculate transient intrinsic viscosity $\langle\eta\rangle$, first the drag force acting on the flat wall is obtained through integrating the shear stress $\sigma(\mathbf{x})$ on moving wall nodes, which is equal to that acting on the fluid nodes that are nearest to the wall nodes. Then the spatially averaged shear stress $\langle\sigma\rangle$ is equal to the drag force divided by the area of the moving flat wall. After $\langle\eta\rangle$ is further averaged in time, $\langle\bar{\eta}\rangle$ is obtained. Here we can see that $\langle\sigma\rangle$ can be regarded as the $\rho\nu_f\langle G_w\rangle$, where $\langle G_w\rangle$ is the strength of the area-averaged shear rate near the wall. Hence, $\langle G_w\rangle$ is directly related to $\langle\eta\rangle$.

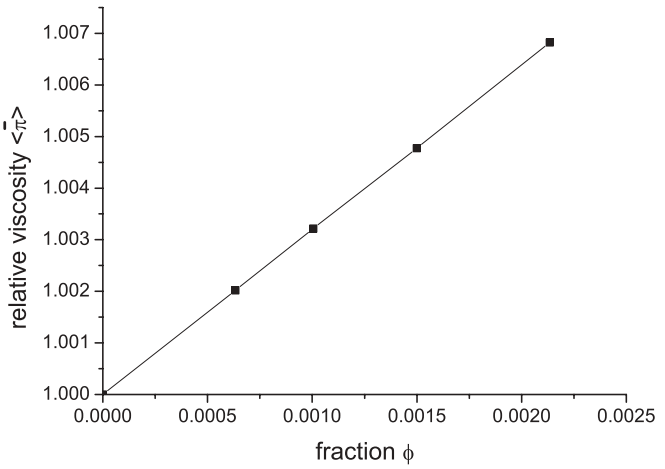

FIG. 2. $\langle\bar{\pi}\rangle$ as a function of volume fraction ϕ for a prolate spheroid with $\varepsilon = 0.8$ and $\mathrm{Re} = 70$.

III. RESULTS AND DISCUSSION

In this section, the intrinsic viscosities for dilute suspensions of ellipsoids are studied. Here our definition of $\langle\bar{\eta}\rangle$ is based on a linear dependence of the relative viscosity $\langle\bar{\pi}\rangle$ at low volume fraction. In the following simulations, we make sure that all the dependences are linear for all cases with different ellipticity ε and Re. One example is shown in Fig. 2. Figure 2 shows the relative viscosity $\langle\bar{\pi}\rangle$ as a function of the volume fraction ϕ. Four cases with different small ϕ are simulated. Through a linear fit of the four points, we can obtain that $\langle\bar{\pi}\rangle = 1 + 3.1929\phi$.

A. Intrinsic viscosity and period

The intrinsic viscosities of dilute suspensions of prolate and oblate spheroids at $\mathrm{Re} = 0.5$ are illustrated in Fig. 3. For the prolate spheroid, the free mode is a tumbling state [15]. To achieve log rolling mode, the x' axis (evolution axis) is constrained tentatively in the x direction. For the oblate spheroid, the log rolling mode is the free mode [15] and it is initiated by fixing the x' axis in the x direction.

Jeffery [5] has given an analytical solution for suspensions of the ellipsoidal particles with different ε. We found that for the suspensions of both prolate and oblate spheroids, our numerical results agree well with Jeffery's analytical solution [5]. From Fig. 3(a), we also found that for the prolate spheroid at each ellipticity, the log rolling mode and tumbling mode have the minimum and maximum analytically predicted viscosities, respectively. By contrast in Fig. 3(b), for the oblate spheroid, the log rolling mode and tumbling mode have the maximum and minimum analytical viscosities, respectively. On the other hand, at small Reynolds number, for the prolate spheroid, the final mode is the tumbling mode [15], which is the mode having the maximum viscosity. For the oblate spheroid, the final free mode is the log rolling mode [15], which also has the maximum viscosity. Hence, our results argue against Jeffery's hypothesis in that, rather than assuming the least energy-dissipating configurations, the simulated particle tends to adopt the mode with maximum dissipation. That is also consistent with the conclusion of Mason *et al.*, which is obtained from the experiments of suspensions of many spherical particles [10].

The periods of the prolate and oblate particles with different ellipticities are illustrated in Fig. 4. The periods are also compared with the analytical solution [5]. The analytical solution is [5] $T = \frac{2\pi(a^2+b^2)}{abG}$. Again, the periods in our simulations agree very well with the analytical ones. Here we can see that the period increases with the ellipticity and it increases much more quickly when $\varepsilon > 0.7$. We note for clarity that in all the LBM results, the time is normalized by $\frac{1}{G}$.

We also notice that Qi and Luo [1] gave relative viscosities for a prolate spheroid at $\mathrm{Re} \approx 0.1$. However, their calculated values seem to be inconsistent with Jeffery's analytical solution. We demonstrate that in the following. In Ref. [1], the parameters of the prolate spheroid are $a = 12\ l.u.$, $b = c = 6\ l.u.$, and the computational domain is $64\ l.u. \times 64\ l.u. \times 64\ l.u.$. The corresponding volume fraction is $\phi = \frac{4}{3}\pi \times 12 \times 6 \times 6/(64 \times 64 \times 64) = 0.69\%$. The relative viscosities are 1.026 and 1.033 for the log rolling state and the tumbling state, respectively [1]. The intrinsic viscosities $\langle\bar{\eta}\rangle = \frac{\langle\bar{\pi}\rangle - 1}{\phi}$ are $\frac{1.026-1}{0.0069} = 3.767$ and $\frac{1.033-1}{0.0069} = 4.781$, respectively. However,

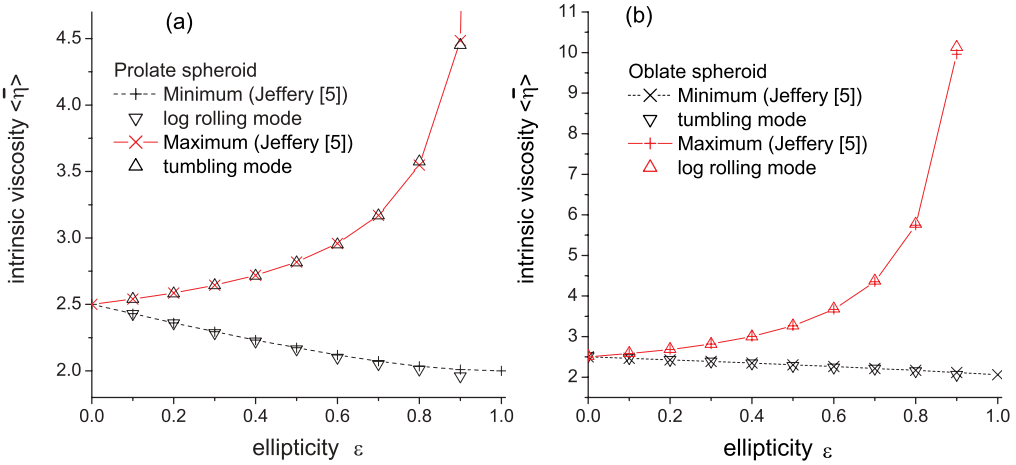

FIG. 3. (Color online) Intrinsic viscosities for dilute suspensions of (a) prolate spheroids and (b) oblate spheroids at $\mathrm{Re} = 0.5$ for different ellipticities.

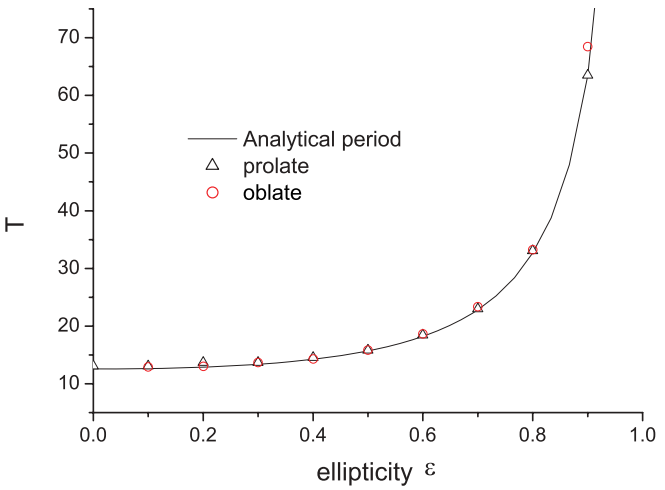

FIG. 4. (Color online) Period T for the prolate and oblate spheroidal particles at Re $= 0.5$ for different ellipticity.

according to Jeffery's study, the minimum and maximum $\langle\bar{\eta}\rangle$ should be 2.174 and 2.819, respectively [5]. Hence, the numerical results for $\varepsilon = 0.5$ in the study of Qi and Luo [1] have large discrepancies with Jeffery's study [5]. It is worth noting that although the results of Ref. [1] are somewhat different from Jeffery's solution, the ratio of the minimum and maximum values is consistent with that solution. It is possible that the present interpretation of the results in Ref. [1] is not completely correct, perhaps due to missing or incorrect information in Ref. [1].

B. Transient property

For the log rolling mode, the intrinsic viscosity would reach a constant value when the flow becomes steady, i.e., the angular velocity of the spheroid becomes constant. However, for the tumbling mode, the transient intrinsic viscosity $\langle\eta\rangle$ is not a constant in a period of rotating and it varies with the particle's orientation. The orientation is described by angles α, β, and γ, which denote the angles between the x' axis and the space-fixed x, y, and z axes, respectively ($\cos^2\alpha + \cos^2\beta + \cos^2\gamma = 1$). The typical variations of the transient intrinsic viscosity as a function of $\cos\beta$ for the dilute suspension of prolate spheroids at Re $\sim$ O(1) and Re $\sim$ O(10) are shown in Fig. 5. The arrows in the figure demonstrate the chronological order. Here we can see that there are two peaks and two valleys in a period when the Reynolds number is low [Fig. 5(a)] while there is only one maximum and one minimum in a period at Re $\sim$ O(10). For dilute suspension of oblate spheroids, similar behavior is also observed. In the following, the mechanics for such different behaviors at low and larger Re will be explored.

First, we would like to discuss the case of low Re. The transient intrinsic viscosity, $\langle\eta\rangle$, the angular velocity in the x direction, ω, and the torque and orientation as functions of t for the suspension of prolate spheroids with Re $= 0.1$ and $\varepsilon = 0.5$ are shown in Fig. 6. Note that the angular velocity is normalized by G and the torque is normalized by $m(Ga)^2$. In the figure, to elucidate more clearly, the times A to E are labeled in chronological order. The time from A to E is a half-period of the tumbling state. In the discussion, we will focus on the orientation and the torque (or the distance-averaged force). The two features may affect the intrinsic viscosity significantly.

From the figure, we can see that when the major axis (x' axis) of the spheroid is parallel to the z axis, $\langle\eta\rangle$ reaches a valley with a value of about 2.51 at $t = 12.3$ (point A). At this orientation, the particle has a minimum effect on $\langle G_w\rangle$, and hence $\langle\eta\rangle$, compared to the other orientations. The particle rotates counterclockwise (refer to Fig. 1, view in the $-X$ direction). When the x' axis approaches the y axis, $\langle\eta\rangle$ increases to a peak value about 3.37 at $t = 15.4$ (point B). At this orientation, the torque increases to a maximum value. From A to B, the torque is positive, which means that it would push the particle to rotate counterclockwise. At point B, the particle strongly hinders the Couette flow and the shear rate near the moving walls is the strongest. After point B, the torque decreases to a negative value, which means the hindering effect becomes weak. Consequently, $\langle\eta\rangle$ becomes smaller and reaches its second valley with $\langle\eta\rangle = 2.65$ at $t = 16.4$ (point C). After point C, the torque acting on the particle increases and hence $\langle\eta\rangle$ increases. On the other hand, the x' axis becomes closer to the z axis. That means the effect of the suspended particle on the shear rate near the moving walls, i.e., $\langle G_w\rangle$,

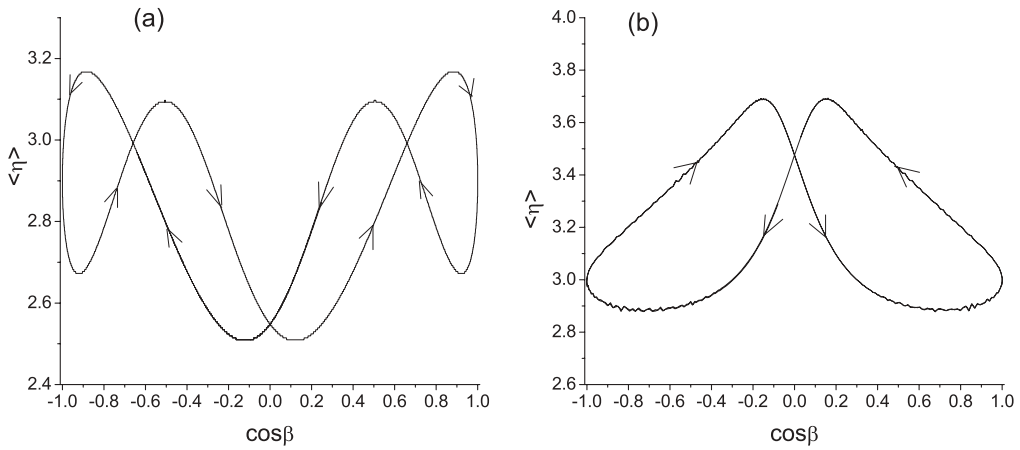

FIG. 5. Transient intrinsic viscosity $\langle\eta\rangle$ as a function of $\cos\beta$ for a dilute suspension of prolate spheroids, (a) a case of low Reynolds number (Re $= 0.5$, $\varepsilon = 0.5$) and (b) a case of larger Reynolds number (Re $= 20$ with $\varepsilon = 0.7$).

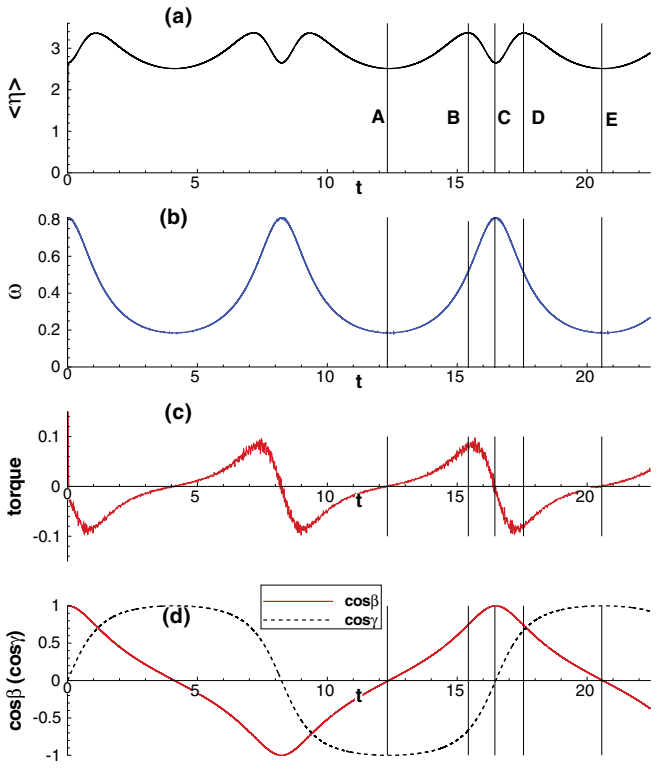

FIG. 6. (Color online) (a) Transient intrinsic viscosity $\langle\eta\rangle$, (b) angular velocity ω, (c) torque, and (d) orientation as functions of time for a dilute suspension of prolate spheroids at Re $= 0.1$ with $\varepsilon = 0.5$.

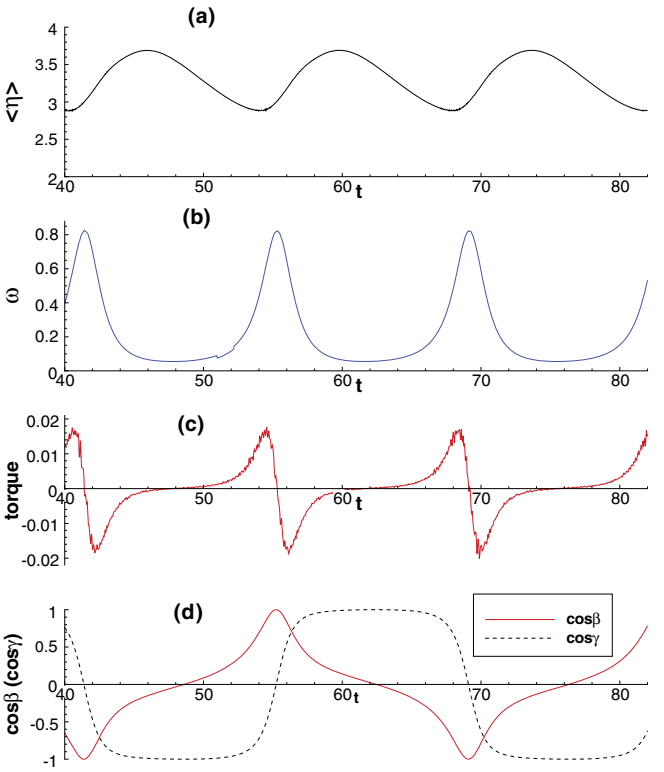

FIG. 7. (Color online) (a) Transient intrinsic viscosity $\langle\eta\rangle$, (b) angular velocity ω, (c) torque, and (d) orientation as functions of time for a dilute suspension of prolate spheroids at Re $= 20$ with $\varepsilon = 0.7$.

becomes smaller. Due to the combination of the above two features, $\langle\eta\rangle$ reaches a second maximum of 3.37 at point D and later $\langle\eta\rangle$ decreases to the minimum value when the x' axis is parallel to the z axis.

Figure 7 shows typical variations of the intrinsic viscosity, angular velocity, torque, and orientation as functions of time when Re $= 20$ and $\varepsilon = 0.7$. In a half-period, there is only one maximum value. The variation of $\langle\eta\rangle$ becomes simpler than that in the low-Re case. From the figure, we can see that at $t \approx 49$, $\cos\beta = 0$ and the x' axis is parallel to the z axis. In this orientation, $\langle\eta\rangle$ should reach its minimum value because the particle has a minimum effect on the intrinsic viscosity if the inertia of the fluid is neglected. However, it takes until $t \approx 55$ before $\langle\eta\rangle$ reaches its minimum value. Hence, the change of $\langle\eta\rangle$ is not synchronous with the change of the orientation of the particle. We also found that the phase lag between $\langle\eta\rangle_{\min}$ and orientation depends on Re.

Typical curves of phase lag are shown in Fig. 8. From the figure, we can see that the phase lag χ/π of prolate spheroids with $\varepsilon = 0.7$, 0.8, and 0.9 increases with Re until Re $\approx$ Re$_a$ and then it decreases. Re$_a$ depends on ε. For $\varepsilon = 0.7$, 0.8, and 0.9, the Re$_a$'s are approximately 100, 60, and 30, respectively. The dashed line in the figure is a line connecting the Re$_a$ for different ε. There are two factors that may affect the phase lag between $\langle\eta\rangle_{\min}$ and $\cos\beta = 0$: the particle inertia and the fluid inertia. Note that even when the inertia of the fluid is small, i.e., when Re is small, the inertia of the particle exits. We note that the nondimensional maximum torque acting on the particle decreases with Re (not shown here). This means the inertia of the particle decreases with Re. On the other hand, the inertia of the fluid increases with Re. The competition between the two factors results in the behavior of the phase lag. In the next section, we show that when Re $<$ Re$_a$, both the intrinsic viscosity and the period change linearly with Re, while for Re $>$ Re$_a$, they change nonlinearly with Re.

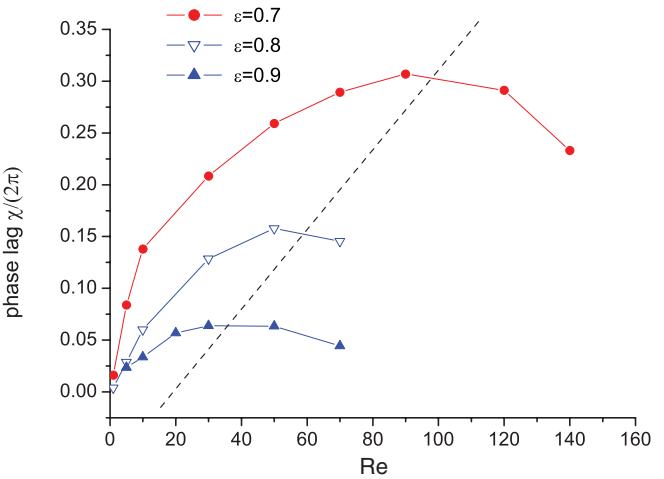

FIG. 8. (Color online) Phase lag between the minimum intrinsic viscosity $\langle\eta\rangle_{\min}$ and $\cos\beta = 0$ for dilute suspensions of prolate spheroids ($\varepsilon = 0.7$,0.8,0.9) as functions of Re.

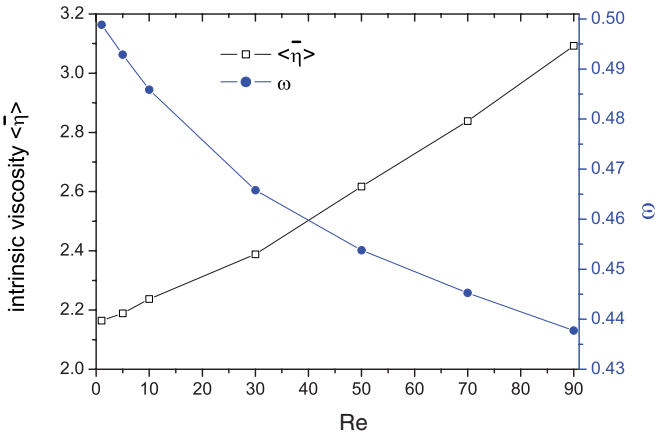

FIG. 9. (Color online) Intrinsic viscosity $\langle\bar{\eta}\rangle$ and angular velocity ω for dilute suspensions of prolate spheroids ($\varepsilon = 0.5$) as functions of Re when the spheroid is constrained into the log rolling mode.

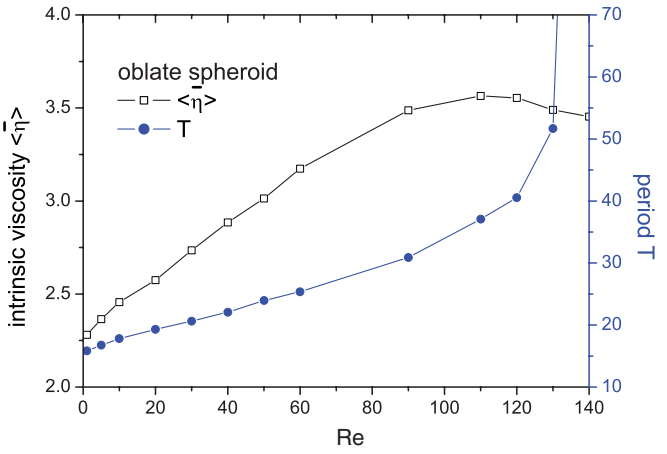

FIG. 10. (Color online) The intrinsic viscosity $\langle\bar{\eta}\rangle$ and period T as functions of Re for the dilute suspension of the tumbling oblate spheroid ($\varepsilon = 0.5$).

C. Re effect on intrinsic viscosity and period

In the study of Huang *et al*. [15], it is found that for a given dynamical mode, the relative viscosity increases with Re when Re < 18. Here we extend the study to higher Re and propose a scaling law for Re $\sim$ O(10).

For the tentatively constrained spheroid, the x' axis always overlaps the x axis and the intrinsic viscosity and equilibrium angular velocity would change with Re. That is illustrated in Fig. 9. When Re increases from 0.5 to 90, The angular velocity ω would decrease from 0.5 to about 0.44 for the prolate spheroid with $\varepsilon = 0.5$. That may be due to the particle and fluid inertia. We note that the angular velocity $\omega = 0.5$ is also observed in the study of a spherical particle in shear flows by Nirschl *et al*. [22]. Here we found that $\langle\bar{\eta}\rangle$ would increase from 2.17 to 3.09. The possible reason is that the shear flow near the particle would be retarded when the equilibrium angular velocity becomes smaller at large Re. That may increase the shear rate near the walls. For the oblate spheroid, a similar variation with Re was also observed.

For the tumbling state, the scaling of the period of rotation is [13] $T = C(\mathrm{Re}_c - \mathrm{Re})^{-\frac{1}{2}}$, where Re_c is the critical Re when the spheroid would stop rotating. However, we found that Re_c depends slightly on the confinement ratio $\frac{L}{b}$. In the following simulation for an oblate spheroid with $\varepsilon = 0.5$, Re_c is about 140. The intrinsic viscosity and period as functions of Re are shown in Fig. 10. We can see that the period increases with Re. For the larger Re near to Re_c, the period seems close to the scaling law found by Aidun *et al*. [13]. Here we found that $T = 220(\mathrm{Re}_c - \mathrm{Re})^{-\frac{1}{2}}$ fits the high-Re section well. However, in the lower Re section, T increases linearly with Re.

For the prolate spheroid, the situation is similar to that of the oblate spheroid. Figure 11 shows the intrinsic viscosity and period as functions of Re for the prolate spheroid. Both $\langle\bar{\eta}\rangle$ and T change almost linearly with Re when Re $< \mathrm{Re}_a$. When Re $> \mathrm{Re}_a$, both $\langle\bar{\eta}\rangle$ and T change nonlinearly with Re. From Fig. 11, we can see that for $\varepsilon = 0.7$, 0.8, and 0.9, there is a critical Reynolds number Re_c, beyond which the period of rotation would become infinite, i.e., the particle would stop and remain stationary in the flow. The corresponding Re_c's are approximately 167, 120, and 75, respectively. Hence, Re_c decreases with the ellipticity ε. For $\varepsilon = 0.5$, due to numerical instability, we have not been able to carry out simulations of cases with Re > 500. At Re ≈ 500, we did not observe the stationary state for cases of $\varepsilon = 0.5$. It is believed that for $\varepsilon = 0.5$, they have similar behavior as $\varepsilon = 0.7$, 0.8, and 0.9. The difference is that Re_a and Re_c are much larger than those of $\varepsilon = 0.7$, 0.8, and 0.9. Here only cases Re < 200 for $\varepsilon = 0.5$ are illustrated.

First we analyze the linear dependence of $\langle\bar{\eta}\rangle$ and T on Re (Re $< \mathrm{Re}_a$). In Fig. 11, the solid lines are the linear fits. From Fig. 11(a), we can see that for $\varepsilon = 0.5$ and 0.7, $\langle\bar{\eta}\rangle$ increases with Re. However, for $\varepsilon = 0.8$ and 0.9, $\langle\bar{\eta}\rangle$ decrease with Re. However, in Fig. 11(b), for all ε, the period increases with Re. For Re $< \mathrm{Re}_a$, the scaling law is

$$\langle\bar{\eta}\rangle = \langle\bar{\eta}_0\rangle + \kappa_1 \mathrm{Re}, \quad T = T_0 + \kappa_2 \mathrm{Re}, \tag{8}$$

TABLE I. Slopes of the linear fit for the $\langle\bar{\eta}\rangle$-Re and T-Re curves (dilute suspensions of tumbling prolate spheroids).

Ellipticity ε	$\langle\bar{\eta}_0\rangle$	κ_1 (slope of the $\langle\bar{\eta}\rangle$-Re curve)	T_0	κ_2 (slope of the T-Re curve)
0.0	2.5	0.0253	12.57	0.072
0.3	2.641	0.0194	13.69	0.096
0.5	2.738	0.0130	17.06	0.117
0.7	3.116	0.002 87	22.49	0.232
0.8	3.443	−0.003 37	31.72	0.417
0.9	4.482	−0.0201	58.83	1.069

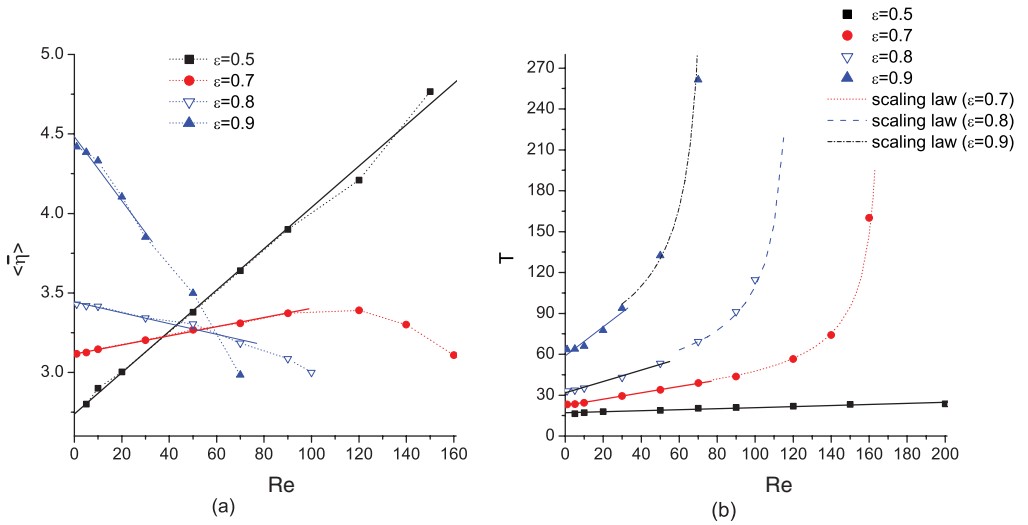

FIG. 11. (Color online) (a) The intrinsic viscosity $\langle\bar{\eta}\rangle$ and (b) period T as functions of Re for dilute suspensions of tumbling prolate spheroids. Solid lines represent the linear fit of the data in the section of $\mathrm{Re} < \mathrm{Re}_a$.

where $\langle\bar{\eta_0}\rangle$ and T_0 should be very close to the analytical intrinsic viscosity and period [5], which totally neglect inertial effects. κ_1 and κ_2 are the slopes of the $\langle\bar{\eta}\rangle$-Re and T-Re curves, respectively, which depend on ε. For the tumbling prolate spheroids, κ_1 and κ_2 for different ε are illustrated in Table I. From the table, we can see that the slope of the $\langle\bar{\eta}\rangle$-Re curve decreases with ε. In contrast, the slope of the T-Re curve increases with ε.

Next we would like to discuss the nonlinear dependence of $\langle\bar{\eta}\rangle$ and T on Re when $\mathrm{Re} > \mathrm{Re}_a$. For the nonlinear regime of each $\langle\bar{\eta}\rangle$-Re curve, a second-degree polynomial fit seems appropriate. For $\varepsilon = 0.7$, 0.8, and 0.9, the formulas are $\langle\bar{\eta}\rangle = 2.117 + 0.0239\,\mathrm{Re} - 1.105 \times 10^{-4}\mathrm{Re}^2$, $\langle\bar{\eta}\rangle = 2.748 + 0.0149\,\mathrm{Re} - 1.236 \times 10^{-4}\mathrm{Re}^2$, and $\langle\bar{\eta}\rangle = 4.077 - 0.0015\,\mathrm{Re} - 2.017 \times 10^{-4}\mathrm{Re}^2$, respectively. The scaling law of the period [13], i.e., $T = C(\mathrm{Re}_c - \mathrm{Re})^{-\frac{1}{2}}$, is considered next. For $\varepsilon = 0.7$, 0.8, and 0.9, the corresponding nonlinear fits are $T = 390(167 - \mathrm{Re})^{-\frac{1}{2}}$, $T = 490(120 - \mathrm{Re})^{-\frac{1}{2}}$, and $T = 650(75 - \mathrm{Re})^{-\frac{1}{2}}$, respectively. They are also shown in Fig. 11(b). The Re_c's are consistent with our numerical simulations because when $\mathrm{Re} > \mathrm{Re}_c$, the particle is found to remain stationary in a certain orientation.

IV. CONCLUSIONS

The shear viscosity of dilute suspensions of ellipsoidal particles is studied using a MRT LBM at finite Re. In the investigation of energy dissipation at $\mathrm{Re} = 0.5$, the maximum and minimum intrinsic viscosities obtained from LBM are highly consistent with the analytical solution of Jeffery. On the other hand, our results invalidate Jeffery's hypothesis [5] about the particle modes self-organizing to minimize energy dissipation.

At low Re, the temporal variation of transient intrinsic viscosity in a period is more complex than that at high Re. The orientation and the torque or the average force acting on the particle are found to affect the transient behavior of $\langle\eta\rangle$. The inertial effects of the particle and fluid contribute to the phase lag between $\langle\eta\rangle$ and the orientation of the particle. At lower Re, the phase lag increases with Re. When Re approaches a critical Reynolds number Re_a, the phase lag begins to decrease with Re. The Re_a is ellipticity-dependent.

The intrinsic viscosity and period as functions of Re are also investigated. For the elliptical spheroids, in the low-Re regime ($\mathrm{Re} < \mathrm{Re}_a$), both $\langle\bar{\eta}\rangle$ and the period change linearly with Re. For the linear fit in the low-Re regime, the slopes of the $\langle\bar{\eta}\rangle$-Re and T-Re curves change monotonically with ellipticity ε. In the high-Re regime ($\mathrm{Re} > \mathrm{Re}_a$), the dependence of T on Re is consistent with the scaling law proposed by Aidun *et al.* [13], and the dependence of $\langle\bar{\eta}\rangle$ on Re is described well by a second-degree polynomial.

ACKNOWLEDGMENTS

H.H. is supported by the National Natural Science Foundation of China (NSFC) (Grant No. 11172297). The authors thank M. C. Sukop and Junjie Huang, who read through the paper carefully and gave many good suggestions.

[1] D. W. Qi and L. S. Luo, J. Fluid Mech. **477**, 201 (2003).
[2] A. Einstein, *Investigations on the Theory of Brownian Movement* (Dover, New York, 1975); Ann. Phys. **34**, 591 (1911).
[3] J. M. Krieger and T. J. Dougherty, Trans. Soc. Rheol. **3**, 137 (1959).
[4] S. V. Lishchuk, I. Halliday, and C. M. Care, Phys. Rev. E **74**, 017701 (2006).
[5] G. B. Jeffery, Proc. R. Soc. London, Ser. A **102**, 161 (1922).
[6] L. G. Leal, J. Fluid Mech. **69**, 305 (1975).
[7] L. G. Leal, Annu. Rev. Fluid Mech. **12**, 435 (1980).

[8] G. I. Taylor, Proc. R. Soc. Lond. A **103**, 58 (1923).
[9] A. Karnis, H. L. Goldsmith, and S. G. Mason, Nature (London) **200**, 159 (1963).
[10] A. Karnis, H. Goldsmith, and S. G. Mason, Can. J. Chem. Eng. **44**, 181 (1966).
[11] J. F. Brady and G. Bossis, Annu. Rev. Fluid Mech. **20**, 111 (1988).
[12] J. Feng and D. D. Joseph, J. Fluid Mech. **303**, 83 (1995).
[13] C. K. Aidun, Y. N. Lu, and E. J. Ding, J. Fluid Mech. **373**, 287 (1998).
[14] E. Ding and C. K. Aidun, J. Fluid Mech. **423**, 317 (2000).
[15] H. Huang, X. Yang, M. Krafczyk, and X.-Y. Lu, J. Fluid Mech. **692**, 369 (2012).
[16] Z. Yu, N. Phan-Thien, and R. I. Tanner, Phys. Rev. E **76**, 026310 (2007).
[17] C. J. Lin, J. H. Peery, and W. R. Schowalter, J. Fluid Mech. **44**, 1 (1970).
[18] P. Lallemand and L.-S. Luo, J. Comput. Phys. **184**, 406 (2003).
[19] D. d'Humiéres, I. Ginzburg, M. Krafczyk, P. Lallemand, and L.-S. Luo, Trans. R. Soc. London A **360**, 437 (2002).
[20] R. Mei, D. Yu, W. Shyy, and L.-S. Luo, Phys. Rev. E **65**, 041203 (2002).
[21] O. Filippova and D. Hanel, J. Comput. Phys. **147**, 219 (1998).
[22] H. Nirschl, H. A. Dwyer, and V. Denk, J. Fluid Mech. **283**, 273 (1995).